

Title	Mo doped TiO ₂ : impact on oxygen vacancies, anatase phase stability and photocatalytic activity
Authors	Kumaeavel, Vignesh;Rhatigan, Stephen;Mathew, Snehamol;Michel, Marie Clara;Bartlett, John;Nolan, Michael;Hinder, Steven;Gascó, Antonio;Ruiz-Palomar, César;Hermosilla, Daphne;Pillai, Suresh
Publication date	2020-02-10
Original Citation	Vignesh, K., Stephen, R., Snehamol, M., Marie Clara, M., John, B., Michael, N., Steven, H., Antonio, G., César, R.-P., Daphne, H. and Suresh, P. (2020) 'Mo doped TiO ₂ : impact on oxygen vacancies, anatase phase stability and photocatalytic activity', Journal of Physics: Materials, doi: 10.1088/2515-7639/ab749c
Type of publication	Article (peer-reviewed)
Link to publisher's version	http://iopscience.iop.org/10.1088/2515-7639/ab749c - 10.1088/2515-7639/ab749c
Rights	© 2020 The Author(s). Published by IOP Publishing Ltd. As the Version of Record of this article is going to be published on a gold open access basis under a CC BY 3.0 licence, this Accepted Manuscript is available for reuse under a CC BY 3.0 licence immediately. Everyone is permitted to use all or part of the original content in this article, provided that they adhere to all the terms of the licence - https://creativecommons.org/licenses/by/3.0
Download date	2024-04-20 10:34:36
Item downloaded from	https://hdl.handle.net/10468/9708



University College Cork, Ireland
Coláiste na hOllscoile Corcaigh

ACCEPTED MANUSCRIPT • OPEN ACCESS

Mo doped TiO₂: impact on oxygen vacancies, anatase phase stability and photocatalytic activity

To cite this article before publication: Vignesh Kumaeavel *et al* 2020 *J. Phys. Mater.* in press <https://doi.org/10.1088/2515-7639/ab749c>

Manuscript version: Accepted Manuscript

Accepted Manuscript is “the version of the article accepted for publication including all changes made as a result of the peer review process, and which may also include the addition to the article by IOP Publishing of a header, an article ID, a cover sheet and/or an ‘Accepted Manuscript’ watermark, but excluding any other editing, typesetting or other changes made by IOP Publishing and/or its licensors”

This Accepted Manuscript is © 2020 The Author(s). Published by IOP Publishing Ltd.

As the Version of Record of this article is going to be / has been published on a gold open access basis under a CC BY 3.0 licence, this Accepted Manuscript is available for reuse under a CC BY 3.0 licence immediately.

Everyone is permitted to use all or part of the original content in this article, provided that they adhere to all the terms of the licence <https://creativecommons.org/licenses/by/3.0>

Although reasonable endeavours have been taken to obtain all necessary permissions from third parties to include their copyrighted content within this article, their full citation and copyright line may not be present in this Accepted Manuscript version. Before using any content from this article, please refer to the Version of Record on IOPscience once published for full citation and copyright details, as permissions may be required. All third party content is fully copyright protected and is not published on a gold open access basis under a CC BY licence, unless that is specifically stated in the figure caption in the Version of Record.

View the [article online](#) for updates and enhancements.

Mo doped TiO₂: Impact on oxygen vacancies, anatase phase stability and photocatalytic activity

Vignesh Kumaravel ^{a,b*}, Stephen Rhatigan ^c, Snehamol Mathew ^{a,b}, Marie Clara Michel^c, John Bartlett ^{a,b}, Michael Nolan ^{c*}, Steven J. Hinder ^d, Antonio Gascó ^e, César Ruiz-Palomar^f, Daphne Hermosilla ^f, Suresh C. Pillai ^{a,b*}

^a Nanotechnology and Bio-Engineering Research Group, Department of Environmental Science, School of Science, Institute of Technology Sligo, Ash Lane, Sligo, Ireland.

^b Centre for Precision Engineering, Materials and Manufacturing Research (PEM), Institute of Technology Sligo, Ash Lane, Sligo, Ireland.

^c Tyndall National Institute, University College Cork, Lee Maltings, Dyke Parade, Cork, Ireland.

^d The Surface Analysis Laboratory, Faculty of Engineering and Physical Sciences, University of Surrey, Guildford, Surrey, United Kingdom

^e Department of Forest and Environmental Engineering and Management, School of Forest and Natural Environment Engineering, Universidad Politécnica de Madrid, Ciudad Universitaria, Madrid, Spain.

^f Department of Agricultural and Forest Engineering, School of Bioenergy, Agronomic, and Forest Industry Engineering, University of Valladolid, Campus Duques de Soria, Soria, Spain.

E-mail: Kumaravel.Vignesh@itsligo.ie; Pillai.Suresh@itsligo.ie; michael.nolan@tyndall.ie

Abstract:

This work outlines an experimental and theoretical investigation of the effect of molybdenum (Mo) doping on the oxygen vacancy formation and photocatalytic activity of TiO₂. Analytical techniques such as X-ray diffraction (XRD), Raman, X-ray photoelectron spectroscopy (XPS) and photoluminescence (PL) were used to probe the anatase to rutile transition (ART), surface features and optical characteristics of Mo doped TiO₂ (Mo-TiO₂). XRD results showed that the anatase to rutile transition was effectively impeded by 2 mol % Mo doping up to 750 °C, producing 67 % anatase and 33 % rutile. Moreover, the crystal growth of TiO₂ was affected by Mo doping *via* its interaction with oxygen vacancies and the Ti—O bond. The formation of Ti—O—Mo and Mo—Ti—O bonds were confirmed by XPS results. Phonon confinement, lattice strain and non-stoichiometric defects were validated through the Raman analysis. DFT results showed that, after substitutional doping of Mo at a Ti site in

anatase, the Mo oxidation state is Mo^{6+} and empty Mo-*s* states emerge at the titania conduction band minimum. The empty Mo-*d* states overlap the anatase conduction band in the DOS plot. A large energy cost, comparable to that computed for pristine anatase, is required to reduce Mo-TiO₂ through oxygen vacancy formation. Mo^{5+} and Ti^{3+} are present after the oxygen vacancy formation and occupied states due to these reduced cations emerge in the energy gap of the titania host. PL studies revealed that the electron-hole recombination process in Mo-TiO₂ was exceptionally lower than that of TiO₂ anatase and rutile. This was ascribed to introduction of 5*s* gap states below the CB of TiO₂ by the Mo dopant. Moreover, the photo-generated charge carriers could easily be trapped and localized on the TiO₂ surface by Mo^{6+} and Mo^{5+} ions to improve the photocatalytic activity.

Keywords: Photocatalysis; Ceramics; Dopant; XPS; Titania

1. Introduction:

Titanium dioxide (TiO₂) has been identified as an interesting nanomaterial in the 21st century, owing to its promising physical, chemical and optical properties for numerous eco-friendly applications, such as water treatment, air purification, energy production and self-cleaning coatings using solar light (1). The commercialisation of photocatalysis technology has gained significant interest in recent decades. The photocatalysis concept has been successfully established for various commercial products, such as cement (2), air purifier (3), paints (4), water filter (5), deodorisers (6), mosquito repellent fabrics (7), and antimicrobial coatings (8, 9). The most commonly existing crystalline polymorphs of TiO₂ are anatase, rutile and brookite (10-12). Anatase is accepted to be the more active phase of TiO₂ and is preferred by the ceramic industries to fabricate light active antimicrobial indoor building materials such as ceramics, glass, tiles and sanitary surfaces (13, 14). This requires thermal stability of the anatase phase under typical ceramic processing conditions. TiO₂ anatase is mainly fabricated at low calcination temperatures (~500 °C) to prevent the anatase to rutile phase transition (ART) (15-17), which produces the less photo-active rutile phase. The photo-activity of anatase arises from its appropriate band edge positions, electron affinity, ionization potential, and the long lifetime of charge carriers (10, 12, 18). Moreover, transient photo-conductance analysis has revealed that the electron-hole recombination phenomena in anatase (101) phase is much slower compared to rutile (110), which is credited in part to the indirect band gap of anatase (11, 19).

The unit cells of anatase and rutile phases are composed of TiO_6 octahedra with titanium atoms at the centre and oxygen atoms at the vertices (20). Both anatase and rutile have a tetragonal primitive cell with space groups I_{41}/amd for anatase and P_{42}/mmm for rutile (20). The octahedral structures of the anatase crystal has a distorted four edge sharing centre (4 corners and 4 edges), whereas the rutile owns a non-distorted two edge sharing centre (2 corners and 6 edges) (21). The ART phase transformation is believed to occur *via* contraction of the *c*-axis, changes in lattice parameters and structural reformation (breaking and making of bonds) (13, 21). TiO_2 anatase phase is easily prepared at a calcination temperature around 500 °C, owing to its low surface free energy (13, 20). The phase transformation of TiO_2 mostly relies on surface defects (oxygen vacancies, Ti interstitials), crystal strain, particle size, existence of additives or dopants, and calcination conditions (20-22). ART of TiO_2 at high temperature could be controlled by the addition of metal ions, suitable chemical modifiers and an appropriate synthesis method (13). Doping with metal ions is a one of the profitable ways to retard the ART (14, 21, 23-31). Metal ions could improve the thermal stability of TiO_2 through the reduction in contact points, and nucleation sites (32).

Generally, doping of an element with higher oxidation state compared to Ti^{4+} would improve charge carrier separation on the photocatalyst surface (33). Molybdenum (Mo; with a highest oxidation state of Mo^{6+}) as a dopant is inexpensive, non-toxic and has high solubility in the TiO_2 anatase lattice (33). The ionic radius of Mo^{6+} is almost identical to that of Ti^{4+} , being 0.062 nm and 0.068 nm, respectively, and, therefore, Mo^{6+} ions could easily replace Ti^{4+} ions in the anatase crystal lattice (34, 35). This kind of doping would minimise the lattice distortion (35, 36). Mo doping could also generate energy states within the band gap of TiO_2 to enhance the light absorption and minimise the electron-hole recombination (35-37). Khan and Berk suggested that an impurity level of $\text{Mo}^{6+}/\text{Mo}^{5+}$ ($\text{Mo}^{6+} 4d^0 1e^- \rightarrow \text{Mo}^{5+} 4d^1$) could be generated below the conduction band (CB) of TiO_2 . During photoexcitation, electron transition could occur from the 0 2*p* valence band (VB) of TiO_2 into the $\text{Mo}^{6+}/\text{Mo}^{5+}$ impurity level and then to the CB of TiO_2 through $d(\text{Mo}^{5+})$ - $d(\text{Ti})$ transition (38). The photo-induced electrons could initiate the reduction of Ti^{4+} ions to Ti^{3+} states at the surface. Moreover, the calcination process creates oxygen vacancies. The substitution of Mo dopant in the TiO_2 crystal lattice could strongly influence the number of oxygen vacancies due to the charge compensation. The formation of Ti^{3+} surface defects and oxygen vacancies could amplify the photocatalytic efficiency of Mo- TiO_2 *via* creating new energy levels and capturing of CB electrons at the surface after the relaxation process (38).

Kemp and McIntyre (39) investigated the photocatalytic activity of Mo-TiO₂ for the degradation of polyvinylchloride. XRD results revealed that 34 % of TiO₂ anatase content was retained by 1 % Mo doping at a 600 °C calcination temperature. Fisher *et al.* (40) studied the antimicrobial property of Mo-TiO₂ coated films on the soiled surfaces in a beer industry under visible light irradiation. The coatings were fabricated on a stainless steel substratum by a magnetron sputtering ion plating technique with the aim to avoid microbial fouling. The bacterium was selected through the isolation of microorganisms on the soiled surface. Mo-TiO₂ coated films showed 5-log reduction against *Escherichia coli* under dark and light conditions. Mo-TiO₂ coatings could function as a secondary barrier to restrain the microbial contamination. Recently, Miljević *et al.* (33) examined the photocatalytic (coated on glass substrate) and self-cleaning (coated on brick and stone) efficiency of Mo-TiO₂-layer double hydroxide (LDH) nanocomposite coatings under visible light irradiation. The results showed that the photocatalytic and self-cleaning properties of Mo-TiO₂-LDH (Mo/Ti = 0.03 mass ratio) were higher than that of TiO₂-LDH. After 24 h of light irradiation, the water contact angle (WCA) of Mo-TiO₂-LDH coated brick (87°) and stone (36°) was significantly decreased as compared to uncoated brick (105°) and stone (58°), suggesting hydrophilicity of the coating. In another study, Yoon *et al.* (41) reported the photocatalytic activity of transparent Mo-TiO₂ (Mo = 3 at.%) films templated using cellulose nanocrystals (CNCs). The optical analysis showed that the visible light absorption capability of Mo-TiO₂-CNCs was significantly higher than bare TiO₂.

The above studies show that Mo is a potential dopant to improve the photocatalytic performance of TiO₂. Mo doping could influence the surface characteristics, oxygen vacancies, crystallinity and formation of Ti³⁺ centres, however, there is still no comprehensive studies on the antimicrobial activity of high temperature stable anatase Mo-TiO₂. Thus, the focus of the present investigation is to study systematically the influence of Mo doping on the phase stability of anatase, formation of oxygen vacancies, and the photocatalytic activity to show that Mo doping could preserve the anatase content at high calcination temperature and thus enhance the activity of TiO₂. A comprehensive analysis on the relationship between the dopant concentration and the surface characteristics of TiO₂ is discussed. Electron-hole recombination was studied through photoluminescence (PL) spectra. Density functional theory (DFT) calculations were also performed to examine the Mo oxidation state and the formation energy of oxygen vacancies and its role in the oxidation states of the cations and the resulting electronic structure, which is vital for the photocatalytic activity. The photocatalytic activity of Mo-doped anatase was studied using the disinfection of total bacteria in wastewater under UVA-LED

light irradiation. The result demonstrates that Mo is a significant dopant to enhance the photocatalytic activity of TiO₂ anatase.

2. Materials and Methods:

Analytical grade chemicals were used in this study. All the chemicals were used as received without further purification.

Synthesis of Mo-TiO₂:

In a typical procedure to prepare 0.5 mol % Mo-TiO₂, titanium isopropoxide (TTIP; 41.81 ml) was mixed with isopropanol (200 ml) under stirring for 15 min, denoted as solution A. In the meantime, solution B was prepared by mixing 0.1225 g of ammonium molybdate tetrahydrate ((NH₄)₆Mo₇O₂₄·4H₂O) in 200 ml of double distilled water under vigorous stirring for 15 min. Afterwards, solution B was added drop by drop into solution A to initiate the hydrolysis process under stirring for 30 min. The resultant milky white solution was dried at 100 °C for 24 h. The amorphous powders were then calcined at various temperatures (500 °C, 600 °C, 700 °C, 750 °C, and 800 °C) in a muffle furnace with a heating rate of 10 °C/min for 2 h. In a similar fashion, 1 mol %, 1.5 mol % and 2 mol % of Mo-TiO₂ samples were also synthesised. Pure TiO₂ (0 mol % Mo-TiO₂) was synthesised by the same procedure without addition of any Mo precursor.

DFT calculations:

DFT calculations were executed by the VASP 5.4 (42, 43) code, using projector augmented wave (44, 45) (PAW) potentials to describe the core-valence interaction. The exchange-correlation functional is estimated by the Perdew-Wang functional (PW91) (46). The potentials for titanium (Ti), oxygen (O) and molybdenum (Mo) explicitly account for 12, 6 and 12 valence electrons, respectively. The energy cut-off for the plane wave basis set is 400 eV and the convergence criteria for electronic and ionic relaxations are 10⁻⁴ eV and 0.02 eV/Å. The bulk lattice parameters of the anatase unit cell were computed as: $a = 3.791 \text{ Å}$ and $c = 9.584 \text{ Å}$; these compare with experimental values of $a = 3.785 \text{ Å}$ and $c = 9.514 \text{ Å}$ (47). A (3 × 3 × 1) anatase supercell, with 108 atoms, was constructed using the computed lattice parameters given above for undoped anatase and Mo was substitutionally doped at a Ti site to give a dopant concentration of 2.8 at. %.

A (3 × 3 × 4) k-point sampling grid was used. The calculations were spin-polarised and no symmetry constraints were imposed. The calculations implemented an on-site Hubbard

correction (DFT+U) (48, 49) to describe the partially filled Ti 3d and Mo 4d states; U = 4.5 eV is applied to Ti 3d states and U = 4.0 eV is applied to Mo 4d with these choices for U informed by previous studies.(50-54)

We considered reduction of Mo-doped TiO₂ via oxygen vacancy formation. To identify the most stable site for vacancy formation, multiple oxygen sites of the Mo-doped structure were considered, taking into account the symmetry of the system. For each oxygen site the vacancy formation energy was computed from the following equation:

$$E^{vac} = E(\text{Mo}_x\text{Ti}_{1-x}\text{O}_{2-y}) + 1/2E(\text{O}_2) - E(\text{Mo}_x\text{Ti}_{1-x}\text{O}_2) \quad (1)$$

Where $E(\text{Mo}_x\text{Ti}_{1-x}\text{O}_{2-y})$ denotes the total energy of Mo-TiO₂ with a single oxygen vacancy. $E(\text{Mo}_x\text{Ti}_{1-x}\text{O}_2)$ represents the total energy of Mo-TiO₂ without an oxygen vacancy. The oxygen vacancy formation energy is referenced to half the total energy of gas-phase O₂.

The oxidation states were analysed through Bader charge analysis (55) and computed spin magnetisations. Given the lack of such analysis in the available literature and to provide benchmark-computed values for the Bader charge of Mo in Mo-TiO₂, calculations were performed on bulk MoO₃ and MoS₂ as reference materials. In the former system, the Bader charge for Mo was computed as 9.2 electrons, to which we ascribe an oxidation state of Mo⁶⁺; for the latter system, the computed Bader charge was 10.7 electrons, corresponding to Mo⁴⁺.

Photocatalytic wastewater disinfection:

The photocatalytic activity of Mo-TiO₂ (0.1 g/L) was assessed by the disinfection of microbes in wastewater (secondary effluent of an urban wastewater (WW) treatment plant, Medinaceli, Soria, Spain) under LED light irradiation with different UVA wavelengths. The characteristics of effluent were determined by the standard method of wastewater analysis (Table S1). The parameters such as pH, conductivity, total volatile solids (TVS), total suspended solids (TSS), chemical oxygen demand (COD), and microbial count (*Escherichia coli*, non coliforms and other coliforms) were measured. Two parallel lines of 10 UVA LED lights (Seoul Viosys, Republic of Korea) of particular wavelength (385 and 395 nm), which were widely scattered to equally cover the reactor surface, was used as the irradiation source. 250 mA of current intensity was used in each LED light setup. This was equivalent to consuming 8.38 W and 8.25 W of electrical power by the 385 nm and 395 nm LED lights, respectively. The lamp was located at a distance of 4.5 cm from the water surface. Under this experimental condition, the actual irradiated power was determined by potassium ferrioxalate actinometry method (56, 57). The results showed that 1682.8 ± 77.1 and 1607.7 ± 56.1 μmol

$\text{m}^{-2} \text{s}^{-1}$ of photons emitted from the 385 and 395 nm LED lights, respectively. All the materials used in this experiment was previously sterilised in an autoclave at 100 °C and 1.5 bar for 40 min. 100 ml of WW was treated in each trial in a glass reactor. 1.0 ml of aliquot was withdrawn from the photo-reactor at regular time intervals (such as 4, 8, 15, 30, 45, and 60 min) to measure the existence of bacteria, in terms of colony-forming units (CFU), by ISO 9308-1:2014 method (58).

At first, 0.5 mL of the WW sample was mixed with 0.5 mL of saline water (0.9 g L^{-1} NaCl in distilled water). Then the samples were filtrated through $0.45 \text{ }\mu\text{m}$ white-gridded mixed cellulose ester filter (GN-6 Metrical®, Pall, New York, USA) in a laminar flow hood to avoid external contamination. Chromocult® agar plates (Millipore, Merck, Darmstadt, Germany) were used as the media to grow the bacterial colonies. CFUs were enumerated after incubating the plates at $36 \pm 2 \text{ }^{\circ}\text{C}$ for 21-24 h. There are three types of colonies may be identified to grow on Chromocult® agar plates such as *Escherichia coli* (dark-blue to violet colour); other coliforms, namely: *Enterobacter aerogenes*, *Citrobacter freundii*, (pink to red colour); and some non-coliform bacteria, namely: *Enterococcus faecalis*, *Pseudomonas aeruginosa* (colourless).

Characterisation:

ART of Mo-TiO₂ was investigated with the help of X-ray diffraction (XRD) and Raman spectroscopy. The crystallinity and phase changes were studied through XRD (Siemens D500) using Cu K α radiation ($\lambda = 0.15418 \text{ nm}$) in the 2θ range of 10° - 80° . Spurr equation was applied to determine the anatase and rutile phase composition as follows:

$$F_R = \frac{1}{1+0.8[I_A(101)/I_R(110)]} \quad (2)$$

Where F_R , $I_A(101)$ and $I_R(110)$ are the rutile phase percentage, intensity of anatase peak and intensity of rutile peak, respectively. Scherrer equation was used to determine the average crystallite size. Raman spectra of Mo-TiO₂ samples were measured for an acquisition period of 3 s with a grating of 300 gr/mm. The surface chemical composition, and the bonding interactions of Mo-TiO₂ were analysed using X-ray photoelectron spectroscopy (XPS) with K-Alpha⁺ spectrometer. Photoluminescence (PL) analysis was recorded to study the effect of Mo doping on the lifetime of charge carriers (excitation wavelength of 350 nm).

3. Results and Discussion:

The lattice oxygen vacancies and the formation of energy levels in Mo-TiO₂ framework were studied *via* DFT calculations. The structural, optical and surface characteristics of Mo-TiO₂ were examined in detail using XRD, Raman, PL and XPS spectra. The phase percentages of Mo-TiO₂ at different calcination temperatures were investigated by XRD. The effect of Mo doping on the changes of TiO₂ lattice parameters were examined *via* Raman spectroscopy. The bonding interactions and oxygen vacancies were studied in detail by XPS and PL. Pure TiO₂ anatase (calcined at 500 °C) and rutile (calcined at 700 °C) were used as reference for comparison.

DFT:

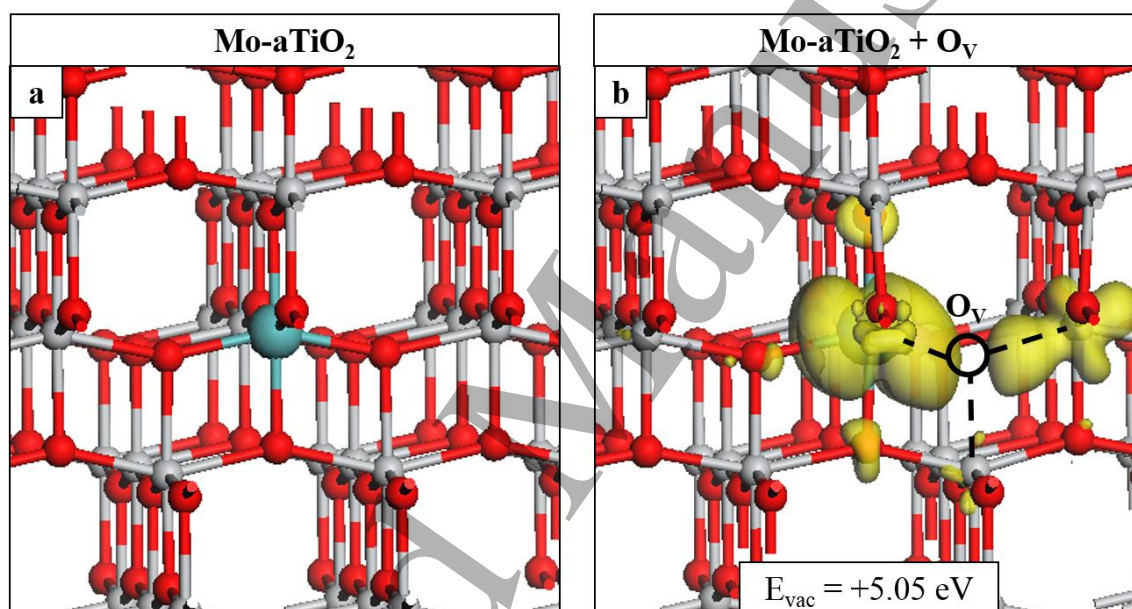


Fig. 1 Relaxed geometry of Mo-doped TiO₂ anatase for (a) stoichiometric Mo-TiO₂ and (b) after formation of a single, reducing oxygen vacancy. The vacancy site sits at an equatorial position relative to the Mo-dopant and the formation energy is included in the inset of panel (b). The yellow iso-surface encloses spin densities of up to 0.02 eV/Å³. The site of the removed O ion is indicated by the black circle and dashed black lines show the ions to which the removed oxygen was bound. In this and subsequent Figures, Ti is represented by grey spheres, O by red and Mo by blue.

The relaxed structure of Mo-doped TiO₂ anatase is shown in Fig. 1(a). The computed Bader charge for Mo is 9.13 electrons, corresponding to Mo⁶⁺ based on comparisons with the Bader charge computed for Mo in bulk MoO₃. Mo-O distances are 1.94 Å and 2.01 Å for oxygen ions in equatorial and apical positions, respectively. These values are almost identical to those computed for Ti-O distances in the undoped supercell, 1.94 Å and 2.00 Å, owing to the similar

1
2
3 ionic radii of Mo^{6+} and Ti^{4+} . Mo-O bond lengths are compared with experimentally determined
4 Ti-O distances of 1.94 Å and 1.96 Å (47), for apical and equatorial oxygen sites.

5
6 We consider reduction of the system *via* oxygen vacancy formation as such defects are
7 implicated in the ART (23, 59-61). The most stable site for the formation of an oxygen vacancy
8 is an equatorial site of the Mo-dopant and the relaxed geometry and excess spin density are
9 shown in Fig. 1(b). The formation energy is 5.05 eV and this is more stable than the next most
10 stable vacancy by 0.1 eV. By comparison, the vacancy formation energy in the undoped anatase
11 supercell is 5.26 eV and so Mo-doping, at this concentration, will not promote vacancy
12 formation to a significant degree.

13
14 After formation of a neutral oxygen vacancy, two electrons are released and these localise
15 in the vicinity of the vacancy site, as shown in the excess spin density plot of Figure 1(b). The
16 computed Bader charge for Mo increases from 9.13 electrons, in the stoichiometric system, to
17 9.91 electrons in the reduced system, indicating reduction to Mo^{5+} . The spin magnetisation in
18 the *d*-orbital of Mo is 1.1 μ_B . For one of the Ti ions to which the removed oxygen was bound,
19 the Bader charge increases from 9.61 to 9.91 electrons. This Ti ion has a computed spin
20 magnetisation of 0.2 μ_B . These results suggest that the excess charge occupies the vacancy site
21 rather than localising at only the Mo and Ti ions (Fig. 1(b)). Typically, Ti^{3+} ions exhibit
22 computed Bader charges of 10.0-10.5 electrons and spin magnetizations of 0.8-1.0 μ_B (23, 62).
23 The values computed for the partially reduced Ti ion in the present work are consistent with
24 our previous study of In-doped TiO_2 (59). This study showed excess charge distributed over
25 the vacancy site in the reduced system, rather than localised at cation sites; the computed Bader
26 charge and spin magnetization for Ti sites neighbouring the vacancy were 9.7/9.8 electrons and
27 0.1/0.2 μ_B , respectively. The excess spin density plot in Fig. 1 (b) shows that the charges are
28 distributed over Mo and Ti and the electron density extends towards the vacancy site.

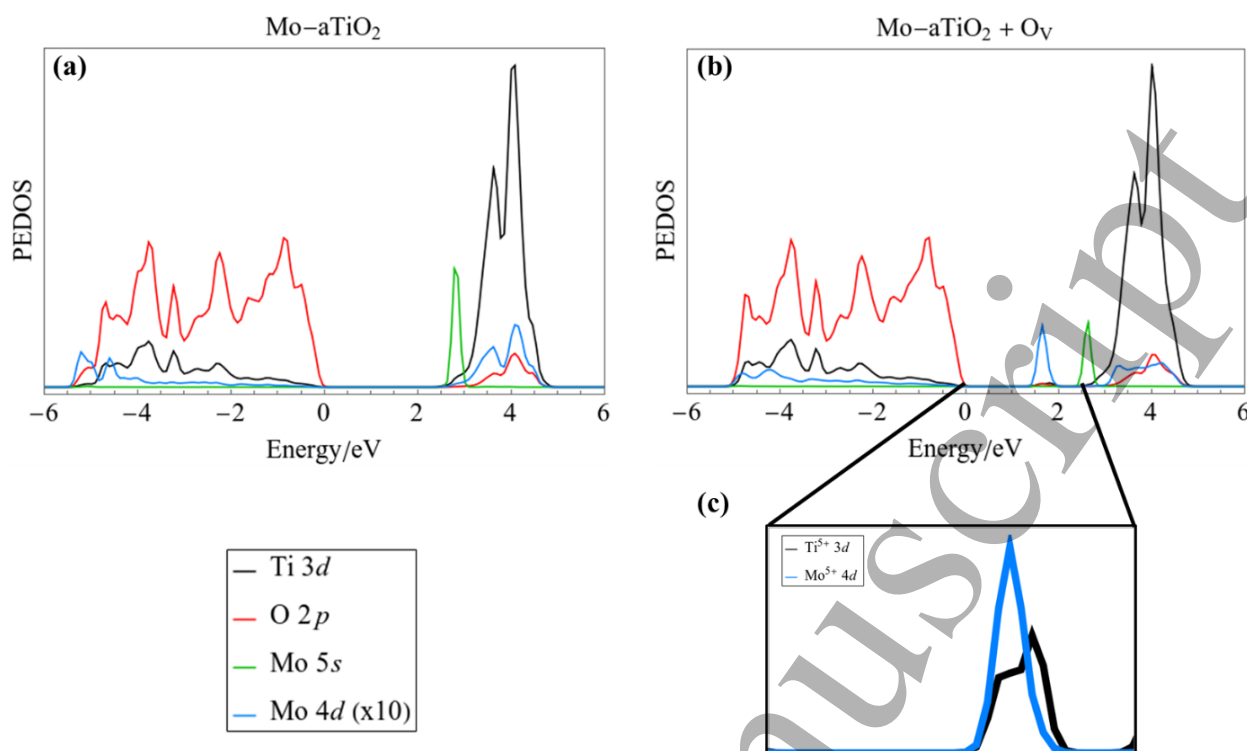


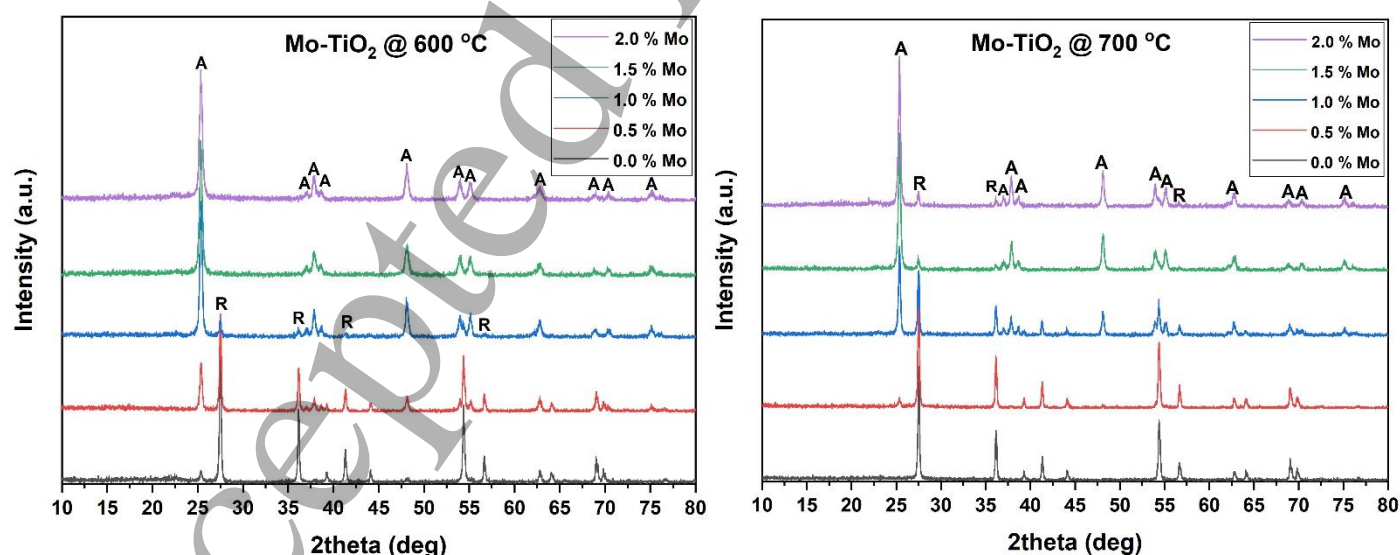
Fig. 2 Computed PEDOS for (a) stoichiometric Mo-doped TiO₂ anatase and (b) reduced Mo-doped TiO₂ anatase, with one oxygen vacancy. Panel (c) shows the occupied Ti³⁺ and Mo⁵⁺ states which emerge in the band gap after vacancy formation.

The projected electronic density of states (PEDOS) were computed for the stoichiometric and reduced system, with one oxygen vacancy, and these are shown in Fig. 2. For the stoichiometric system (Fig. 2(a)), Mo *s*-states emerge at the CBM of the TiO₂ host and the Mo *d*-states overlap with the titania CB. The emergence of Mo-derived defect states below the CBM was reported by the GGA studies of Mo-doped TiO₂ (36, 63). Mo *d*-states below the CBM were identified in these studies but there was no discussion of the Mo *s*-states. In the present work, we find that Mo *d*-states lie above the CBM and this may be ascribed to the implementation of a Hubbard *U* on Mo *d*-states which shifts these states with respect to the TiO₂ CBM. After vacancy formation and reduction of Ti and Mo, occupied Ti and Mo *d*-states emerge in the band gap at 1.65 eV above the valence band maximum (VBM), as shown in Fig. 2(b) and 2(c).

XRD:

XRD patterns of Mo-TiO₂ samples calcined at 600, 700, 750 and 800 °C are shown in Fig. 3. The results revealed that the anatase phase of TiO₂ is significantly preserved up to 750 °C by Mo doping (39) (Table 1). A small red shift is observed for the anatase peak when the Mo

content is increased from 0 to 2 mol %, suggesting the dopant-induced lattice distortion (38). The intensity and width of anatase peaks are strongly influenced by Mo concentration. The average crystallite size of as-synthesised materials is given in Table 2. For 600 °C, the average crystallite size of anatase is decreased with an increase of Mo content, indicating the crystal growth is restrained by Mo content. The existence of Mo ions in the TiO₂ lattice could distribute point defects as heterogeneous nucleation sites, which may restrict the crystal growth (41, 64). Besides, the number of inter-granular contacts between the nearby titania grains may decrease when increasing the concentration of Mo (38). For 700 and 750 °C, the average crystallite size of TiO₂ anatase does not vary much with Mo mol % and the size is increased in some cases such as 1 mol % Mo-TiO₂ (700 °C) and 1.5 mol % Mo-TiO₂ (750 °C). The doping sites of TiO₂ are mainly decided through the ionic radii, coordination number and valence electron of the dopant (65). The ionic radius of Mo⁶⁺ (0.062 nm) is close to that of Ti⁴⁺ (0.068 nm), hence Mo⁶⁺ could easily substitute Ti⁴⁺ ions in the anatase lattice, suggesting changes in lattice parameters and crystal plane distance (65-67). The increase of Mo concentration above 2 mol % results in the formation of molybdenum trioxide (MoO₃). The major peaks of MoO₃ are analogous to those of anatase (101) and rutile (110) peaks. It could be difficult to distinguish the anatase crystalline peaks for samples with high Mo mol % (*e.g.* 4 mol %, 8 mol %, 16 mol %, etc). Consequently, 2 mol % of Mo is sufficient to maintain the anatase percentage of TiO₂ at high calcination temperatures.



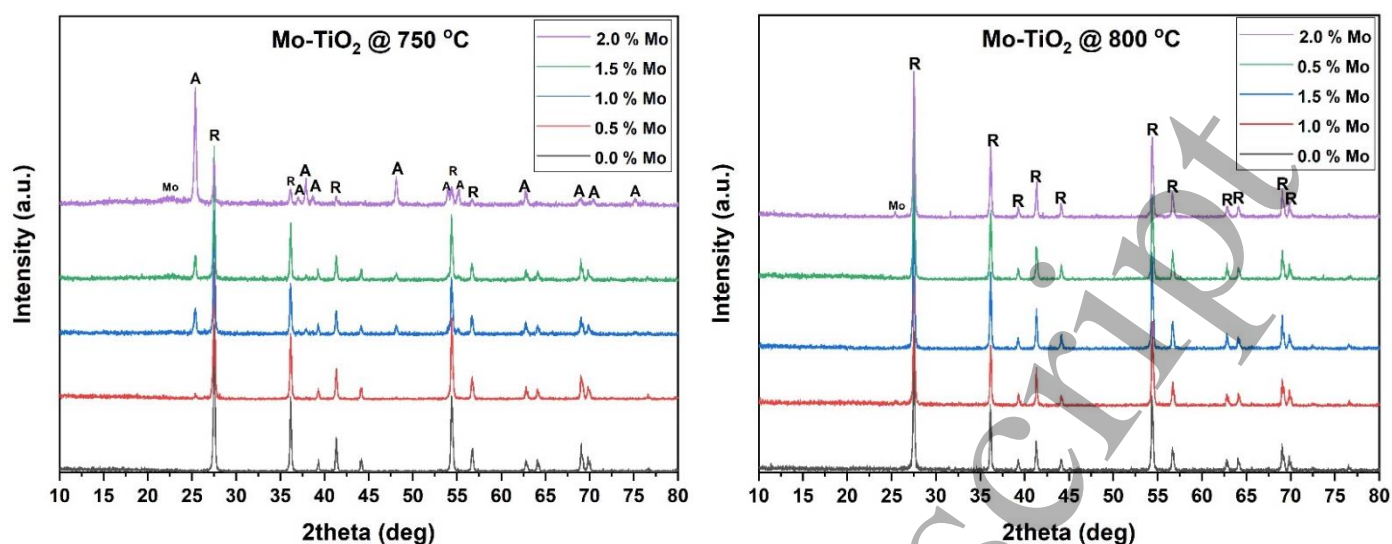


Fig. 3. XRD patterns of Mo-TiO₂ at various calcination temperatures

Table. 1. The phase percentages of Mo-TiO₂ samples calcined at various temperatures

Samples	500 °C		600 °C		700 °C		750 °C		800 °C	
	Anatase	Rutile	Anatase	Rutile	Anatase	Rutile	Anatase	Rutile	Anatase	Rutile
0.0 % Mo-TiO ₂	100	-	7	93	-	100	-	100	-	100
0.5 % Mo-TiO ₂	100	-	30	71	7	93	4	96	-	100
1.0 % Mo-TiO ₂	100	-	84	16	52	48	15	85	-	100
1.5 % Mo-TiO ₂	100	-	100	-	87	13	14	86	-	100
2.0 % Mo-TiO ₂	100	-	100	-	87	13	67	33	-	100

Table. 2. The average crystallite size of Mo-TiO₂

Sample	Temperature (°C)	Particle size (nm)	
		Anatase	Rutile
0.0 % Mo - TiO ₂	600 °C	29.918	35.715
0.5 % Mo - TiO ₂	600 °C	24.908	34.734
1.0 % Mo - TiO ₂	600 °C	23.060	36.316
1.5 % Mo - TiO ₂	600 °C	19.129	-
2.0 % Mo - TiO ₂	600 °C	18.729	-
0.0 % Mo - TiO ₂	700 °C	-	36.234
0.5 % Mo - TiO ₂	700 °C	24.246	36.899
1.0 % Mo - TiO ₂	700 °C	28.0769	35.430
1.5 % Mo - TiO ₂	700 °C	24.469	34.6589
2.0 % Mo - TiO ₂	700 °C	26.248	-
0.0 % Mo - TiO ₂	750 °C	-	36.661
0.5 % Mo - TiO ₂	750 °C	-	36.000
1.0 % Mo - TiO ₂	750 °C	28.0769	36.580
1.5 % Mo - TiO ₂	750 °C	38.0136	33.068
2.0 % Mo - TiO ₂	750 °C	28.0700	36.362

XPS:

The binding interactions and oxidation state of elements in Mo-TiO₂ were analysed by XPS. Ti 2*p*, O 1*s*, Mo 3*d* scans of pure TiO₂ (0 mol % Mo-TiO₂ at 500 °C) and 2 mol % Mo-TiO₂ at 750 °C are displayed in Fig. 4. The representative spin—orbit coupling of Ti 2*p* peaks such as Ti 2*p*_{3/2} and Ti 2*p*_{1/2} are observed at 458.86 eV and 464.53 eV, respectively (Fig. 4(a)) (68, 69). This is ascribed to the existence of titanium in Ti⁴⁺ state. The O 1*s* spectrum of TiO₂ is composed of two peaks. O 1*s* peak is divided into two sub components by peak fitting. The peak located at 530.03 eV is attributed to lattice oxygen in Ti—O bond of TiO₂ (69). The surface O—H group of TiO₂ is detected around 531.94 eV (Fig. 4(b)) (68, 69). The peak positions of Ti 2*p* and O 1*s* are slightly increased for 2 mol % Mo-TiO₂ compared to pure TiO₂ (Fig. 4 (c) and (d)). This is ascribed to high electronegativity of Mo compared to Ti, suggesting a lattice shift by the substitution of Mo⁶⁺ for Ti⁴⁺ ion (34). Oxygen vacancies would also be created by this kind of replacement (34, 68), however, this was not observed in our DFT calculations. Moreover, Mo ions may strongly interact with oxygen atoms or oxygen vacancies *via* chemical bonds in the anatase crystal lattice, suggesting the formation of structural defects such as Ti—O—Mo and Mo—Ti—O bonds by Mo doping (35).

The peaks observed at 233.28 eV and 236.40 eV are accredited to Mo 3*d*_{5/2} and Mo 3*d*_{3/2} of Mo⁶⁺ (Fig. 4 (e)). The sub components detected by peak fitting at 231.84 eV and 235.42 eV are ascribed to Mo 3*d*_{5/2} and Mo 3*d*_{3/2} of Mo⁵⁺. XPS results showed that the percentage of Mo⁶⁺ is higher than that of Mo⁵⁺. The existence of Mo⁵⁺ denotes that the oxygen atoms in the anatase lattice are inadequate to reinforce Mo⁶⁺ ions (35) and based on DFT calculations this is consistent with reduction to Mo⁵⁺ after O_v formation. A gap state (5*s* state of Mo) may be generated below the CB of TiO₂ by Mo doping. This is beneficial to restrain the electron-hole recombination process and prolong the life time of charge carriers. The oxidation-reduction potential of Ti⁴⁺/Ti³⁺ (0.1 eV) is lower than that of Mo⁶⁺/Mo⁵⁺ (0.4 eV) (38). During light irradiation, Mo⁶⁺ could react with photo-induced hole to form Mo⁷⁺, which is highly unstable. Consequently Mo⁷⁺ can further react with surface adsorbed —OH groups to generate ·OH and Mo⁶⁺ (Mo⁷⁺ + OH[−] → Mo⁶⁺ + ·OH) (38).

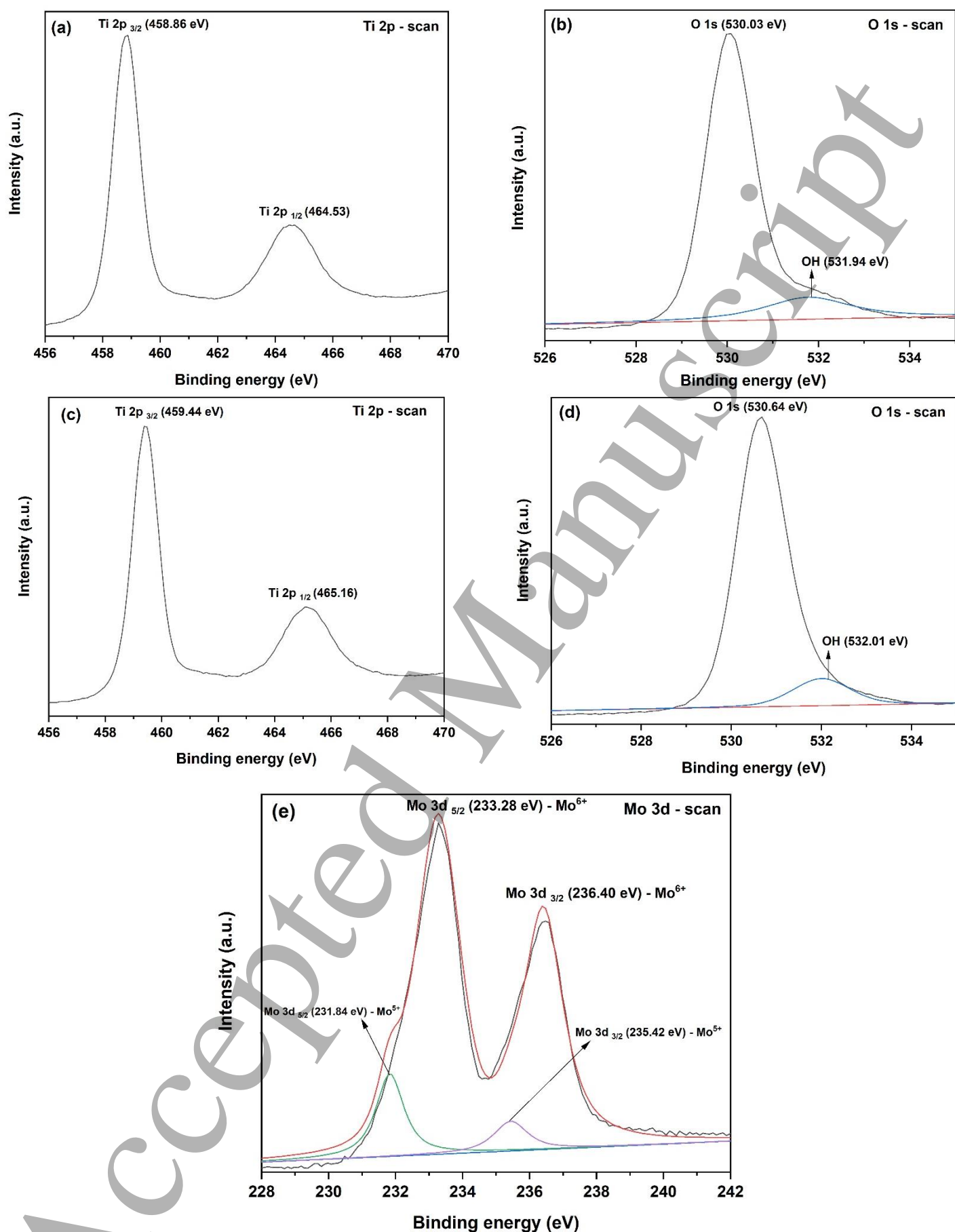


Fig. 4. XPS of 0 mol % Mo-TiO₂ at 500 °C ((a) Ti 2*p* and (b) O 1*s*) and 2 mol % Mo-TiO₂ at 750 °C ((c) Ti 2*p* (d) O 1*s* (e) Mo 3*d*)

Raman spectra:

The effect of Mo doping on the structural changes of TiO₂ anatase was interpreted through Raman spectroscopy. Fig. 5 shows the Raman spectra of pure anatase (0 mol % TiO₂ calcined at 500 °C), rutile (0 mol % TiO₂ calcined at 700 °C) and Mo-TiO₂ samples (calcined at 700 °C and 750 °C). The results showed that Raman modes of TiO₂ anatase are strongly influenced by Mo doping. Raman modes such as E_g, B_{1g}, and A_{1g} are mainly originated from symmetric stretching O-Ti-O, symmetric bending O-Ti-O and anti-symmetric bending O-Ti-O vibrations, respectively (70). Among them, E_g and A_{1g} vibrations are more responsive to oxygen vacancies. Raman active modes of TiO₂ anatase (space group: D¹⁹_{4h} (I₄₁/amd)) and rutile (space group: D¹⁴_{4h} (P₄₂/mnm)) are observed at their corresponding positions. E_g, B_{1g}, A_{1g} or B_{1g} and E_g Raman bands belonging to anatase are observed around 135.02 cm⁻¹, 388.61 cm⁻¹, 508.18 cm⁻¹ and 631.82 cm⁻¹, respectively (Table S2). The significant Raman bands associated with rutile are noted around 439.26 cm⁻¹ and 602.94 cm⁻¹, respectively. As compared to pure anatase, the E_g peaks of Mo-TiO₂ are red shifted with an increase of line width (71). The peak shift is explained by a number of competitive mechanisms, such as phonon confinement, lattice strain/distortion and non-stoichiometric defects due to oxygen vacancies (72-75). The peak broadening of E_g with respect to the concentration of Mo is ascribed to changes in anatase crystal lattice, and the cleavage of vibrational phonon mode (76). According to the Heisenberg uncertainty principle, the phonon momentum of distribution (ΔP) increases when the particle size decreases (73). Consequently, the changes in particle size may influence the phonon frequency of Raman modes, leading to peak broadening (73). As the Mo content is increased, the number of oxygen atoms to create Ti-O bonds is reduced, indicating a decrease in force constant of the bond (73). This could induce a red shift of Raman peak, because the force constant of a band is inversely proportional to its wavenumber (73). Choudhury *et al.* (73) suggested that the red shift is related to the reduced lattice size and diminishing of Ti-O bond. Liu and Syu (77) indicated that the red shift and peak broadening are attributed to oxygen deficiency in the crystal.

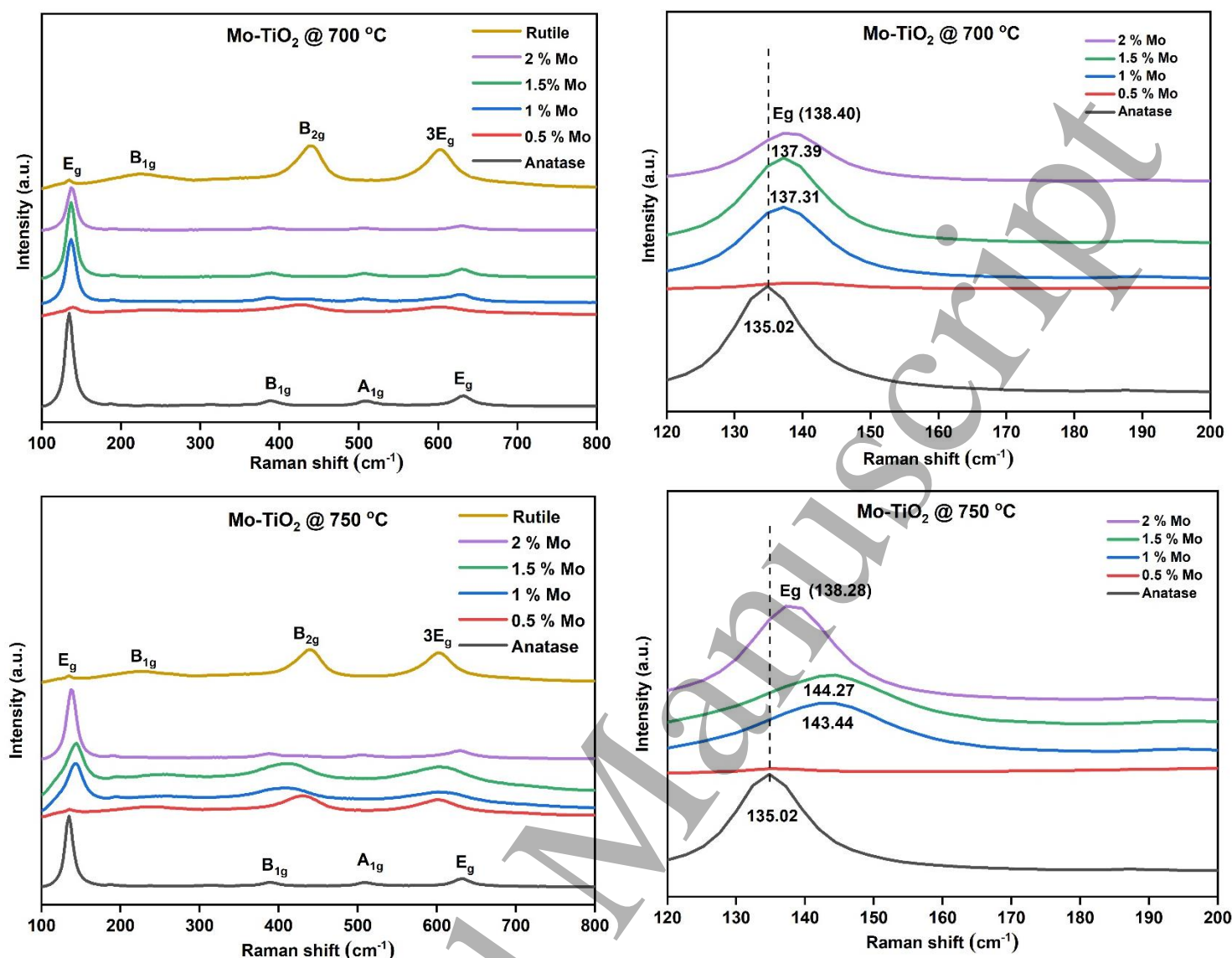


Fig. 5. Raman spectra of (a) and (b) Mo-TiO₂ at 700 °C (c) and (d) Mo-TiO₂ at 750 °C

PL:

PL spectra of Mo-TiO₂ samples calcined at 700 °C are shown in Fig.6. Mechanisms such as electron—hole recombination or separation and electron—phonon scattering are involved in the PL process (78). PL spectrum of TiO₂ anatase primarily originates from oxygen vacancies, surface defects, and self-trapped excitons (78). A peak at *ca.* 380 nm is ascribed to the band—band transition in TiO₂ (79, 80). The characteristic radiative recombination of self-trapped excitons confined within the TiO₆ octahedra and oxygen vacancies is observed as a broad shoulder peak at *ca.* 419 nm (80). The peaks found in the range of 400 – 500 nm originated from the oxygen vacancy related defect centres (80). The blue-green emission peak observed around 485 nm is accredited to the charge transfer from Ti to O atom in TiO₆ octahedra

associated with the oxygen vacancies (78). The peaks at *ca.* 460 nm and 535 nm are correlated to trapped or bound electrons to the oxygen vacancy centres (79). PL peak in the range of 485-490 nm is ascribed to the charge transfer process from Ti^{3+} to oxygen anion in TiO_6^{-8} complex coupled with surface oxygen vacancies (38). The defect states or oxygen vacancy colour centres are denoted as F , F^+ and F^{2+} for two-trapped electrons, one-trapped electron and no-trapped electrons, respectively (79, 80). PL quenching or enhancing mechanism results from the non-radiative oxygen vacancy colour centres. The peaks around 440 nm and 450 nm are associated to F or F^{2+} color centres (80). The dominant peaks around 460 nm and 485 nm are ascribed to F^+ color centre (80).

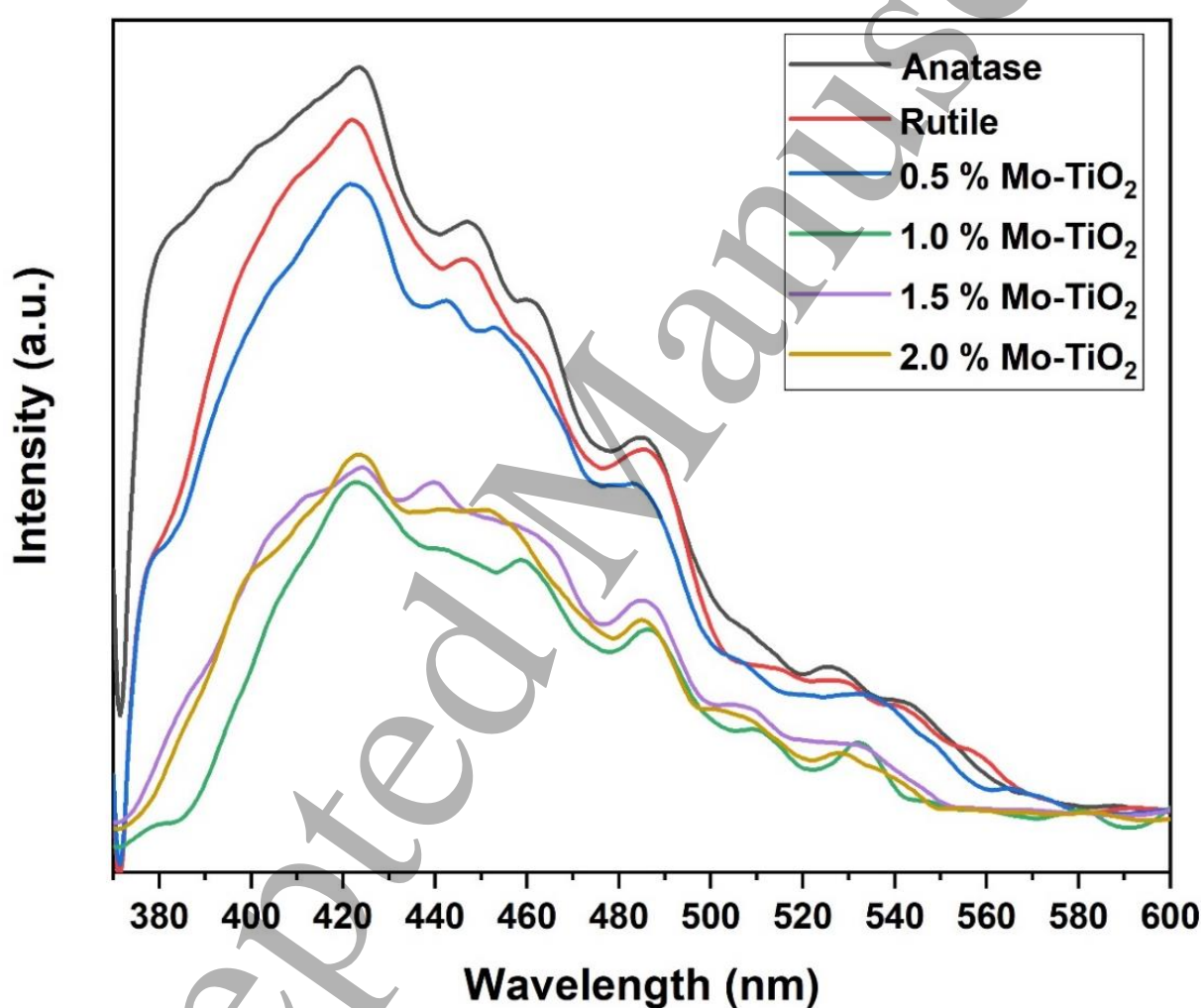


Fig. 6. PL spectra of Mo-TiO₂, anatase and rutile

In our samples, it is clear that the PL emission peaks of pure TiO₂ are quenched by introduction of the Mo dopant. The intensity of the PL peaks of the as-synthesised samples are in the order anatase (0% Mo-TiO₂ at 500 °C) > rutile (0 % Mo-TiO₂ at 700 °C) > 0.5 Mo-TiO₂

$> 2 \text{ Mo-TiO}_2 > 1.5 \text{ Mo-TiO}_2 > 1 \text{ Mo-TiO}_2$. Mo doping can introduce gap states below the CB of TiO_2 and this could suppress the electron-hole recombination process. The effect of Mo concentration on oxygen vacancies is clearly observed in terms of PL peak shift. Ti—O bond in the anatase lattice is disturbed by Mo doping. The impact on oxygen vacancies of TiO_2 could be attributed to the effect of calcination temperature (38). The concentration of oxygen vacancy centres may vary with respect to the concentration of Mo (79). Consequently, the photo-generated electrons could be easily trapped and localised in the oxygen vacancies, reducing the probability of photo-generated electron-hole recombination (79). In addition to oxygen vacancies, the PL intensity could also be influenced through the mobility of carriers (79).

Photocatalytic wastewater disinfection:

The photocatalytic activity of 0 % mol Mo-TiO_2 (calcined at 500 °C) and 2 % mol Mo-TiO_2 (calcined at 750 °C) for the specific removal of total bacteria in WW under 385 nm and 395 nm UVA LED light irradiation is displayed in Fig. 8. The percentages of N/N_0 values were plotted against the irradiation time. N and N_0 are the number of bacteria (CFU/mL) at irradiation time 't' and 0, respectively. The efficiency was denoted by a parameter 'b' (rate coefficient) from the exponential decay curves. In the case of 385 nm LED light, the total bacteria removal for 2 % mol Mo-TiO_2 is ~1.5 times higher than that of TiO_2 . However, the total bacteria removal for 2% mol Mo-TiO_2 is ~2.8 times higher in comparison with pure TiO_2 under 395 nm LED light irradiation. The disinfection efficiency of Mo-TiO_2 is maximal at 395 nm LED light compared to that of 385 nm LED light. The total disinfection was achieved in almost 30 min of LED light irradiation. The high activity of Mo-TiO_2 under 395 nm LED light is attributed to the maximum light absorption with respect to its specific band gap and electronic properties, suggesting the generation of more charge carriers responsible for microbial disinfection (81). The photocatalytic activity could be influenced by the competitive reaction between the microbes and other organic matter existing in the WW (82). Mo doping could enhance the surface active sites and endorse the interfacial charge transfer process (81, 83). The Mo dopant could influence the crystallite size and surface active sites of TiO_2 to promote the adsorption of microbes on the photocatalyst surface (84). The formation gap states by Mo dopant could extend the lifetime of photo-induced charge carriers. The poor disinfection for photolysis experiments is ascribed to the protection of remaining active cells by the metabolites released from the destructed cells (83, 85). The disinfection mechanism of microbes in WW may be attributed to the oxidative degradation of cells by reactive oxygen

1
2
3
4
5
6
7
8
9
10
11
12
13
14
15
16
17
18
19
20
21
22
23
24
25
26
27
28
29
30
31
32
33
34
35
36
37
38
39
40
41
42
43
44
45
46
47
48
49
50
51
52
53
54
55
56
57
58
59
60

species, increase of cell permeability, leakage of minerals, DNA/RNA damage, and inhibition of protein synthesis (83, 86, 87).

Accepted Manuscript

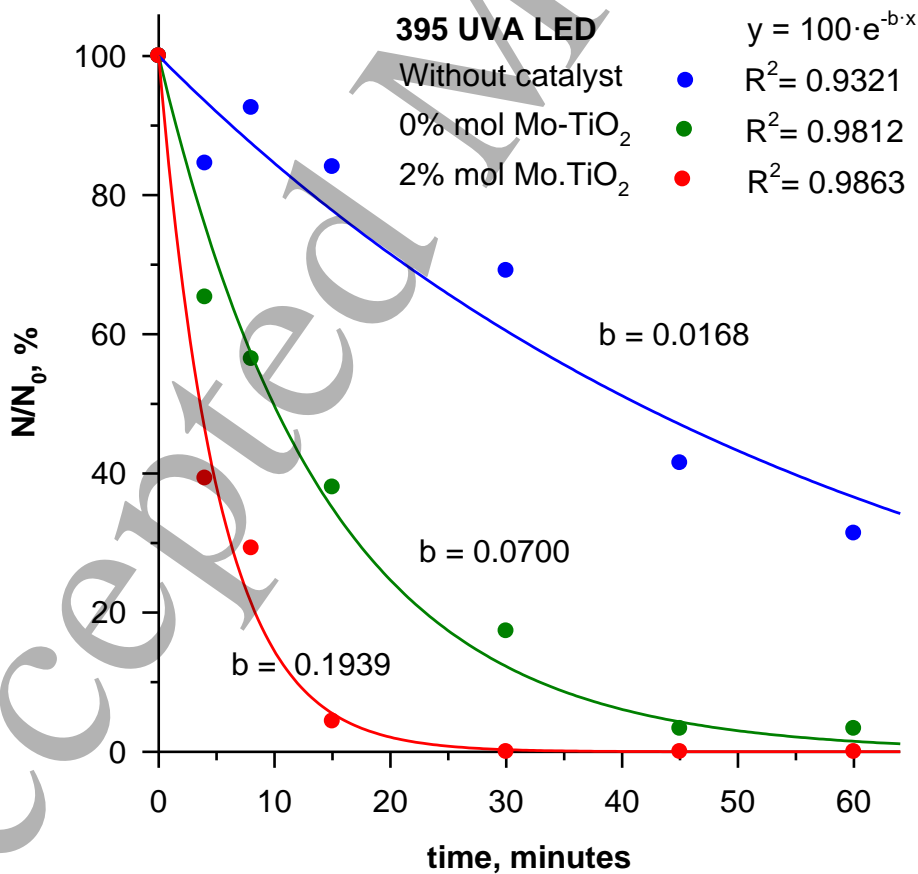
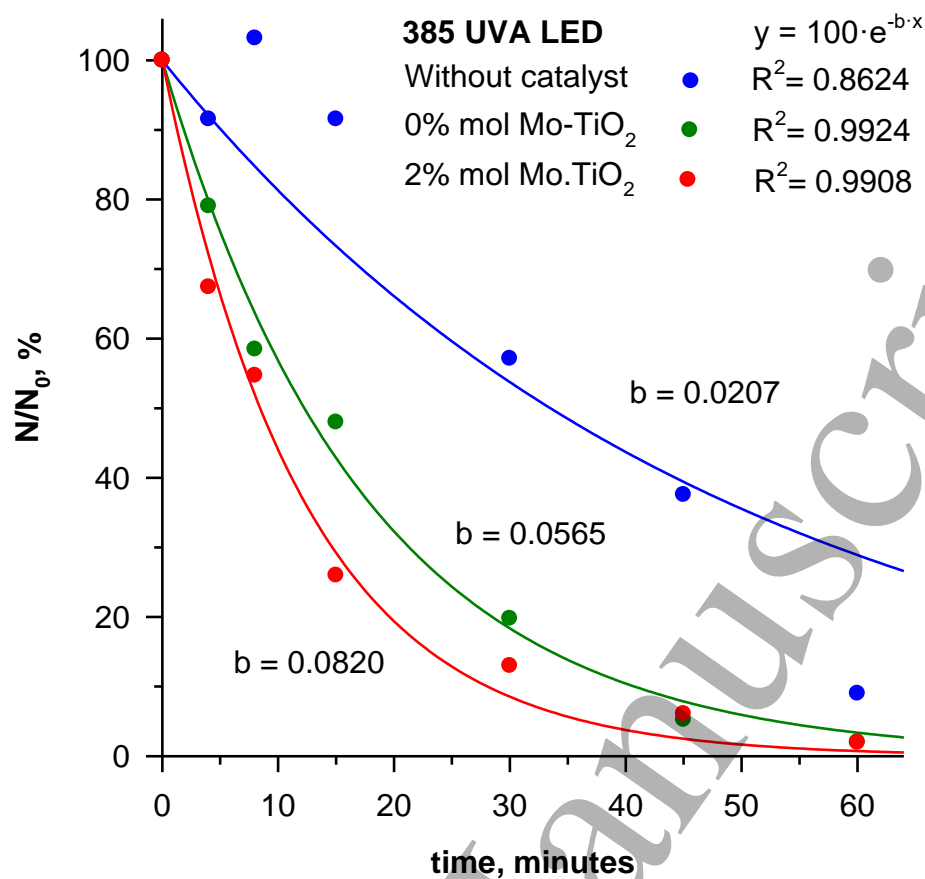


Fig. 7. Photocatalytic disinfection efficiency of TiO₂ and Mo-TiO₂ under UVA LED light irradiation

XRD and Raman analysis clearly validate that the anatase crystal structure of TiO₂ is well sustained after doping with Mo at high calcination temperature. DFT studies showed that gap states (such as *s*- and *d*- states) could be created between the VB and CB of TiO₂, suggesting enhanced charge carrier separation on the photocatalyst surface. Raman analysis suggested that the lattice size and Ti-O bond strength are modified by Mo doping. The formation of oxygen vacancies may be varied with respect to the Mo dopant concentration because of the cleavage of more Ti-O bonds, indicating the contraction of O-Ti-O bond angle (73). The photo-generated electrons could be captured by Mo⁶⁺, impurity levels, Ti³⁺ centres, and shallow or deep traps (38). The trapped electrons would further react with surface adsorbed oxygen to create more reactive oxygen species (38). PL analysis confirmed that the charge carrier mobility would be decreased as they interact with the dopants or defect centres, suggesting enhancement in the charge-carrier separation to improve the photocatalytic activity. Mo doping does not introduce any new peaks in the PL spectrum of TiO₂. Nevertheless, the PL intensity of Mo-TiO₂ peaks are smaller compared to anatase and rutile, suggesting the modification of surface defects and a reduction in the number of recombination centres (38). The photocatalytic activity was tested for the disinfection of microbes in a real WW system rather than using a simulated wastewater system. The disinfection efficiency of Mo-TiO₂ was superior compared to pure TiO₂. The photocatalytic experiments also demonstrated that Mo doping could improve the photon absorption of TiO₂. The high photocatalytic activity of Mo-TiO₂ is accredited to, surface characteristics, crystallinity, formation of gap states, *d-d* electron transition, and the existence of high anatase content (34, 38).

4. Summary:

The effect of Mo doping on oxygen vacancy formation, anatase phase stability and photocatalytic activity of TiO₂ has been successfully investigated. DFT calculations reveal that the Mo dopant is present in anatase as Mo⁶⁺, and is incorporated into the lattice with no distortions to the geometry, due to the similar ionic radii of Mo⁶⁺ and Ti⁴⁺. Analysis of the computed PEDOS plot for the stoichiometric system indicates that Mo 5*s* states emerge below the CBM of TiO₂. The computed energy required for oxygen vacancy formation in Mo-TiO₂ is comparable to that of un-doped anatase and, hence, vacancies should be present in the doped system in similar concentrations to pure anatase, under equivalent preparation conditions. After

vacancy formation, the dopant is reduced to Mo^{5+} and Ti^{3+} is also present. This leads to the emergence of occupied Mo 4d and Ti 3d states in the energy gap. The peak shift in the Raman spectra revealed the influence of oxygen vacancies on the anatase crystal lattice. XPS results show the existence of Mo^{5+} in addition to Mo^{6+} in Mo-TiO₂ samples. The formation of Ti—O—Mo and Mo—Ti—O bonds are also confirmed through XPS analysis. The results also suggest lattice distortions due to substitution of Mo^{6+} for Ti^{4+} ion. The electron transfer process between TiO₂ and surface oxygen vacancies is confirmed by PL analysis. The electron-hole recombination is minimised *via* the appearance of Mo electronic states below the CB of TiO₂. The life time of photo-induced charge carriers is extended through Mo^{6+} , impurity levels, and Ti^{3+} centres. The photocatalytic activity of Mo-TiO₂ was tested with a wastewater from a secondary effluent. The findings suggest that Mo-TiO₂ is an excellent candidate for the fabrication of indoor building materials with light active antimicrobial characteristics.

Acknowledgements:

The authors are thankful to the Renewable Engine (RE) project funded by European Union's INTERREG VA Programme, managed by the Special EU Programmes Body (SEUPB), with match funding provided by the Department of Economy, Department of Jobs, Enterprise and Innovation in Ireland. SR and MN appreciate the support from Science Foundation Ireland (SFI) through the ERA.Net for Materials Research and Innovation (M-ERA.Net 2), SFI Grant Number SFI/16/M-ERA/3418 (RATOCAT) and Horizon 2020 grant (685451). We acknowledge the access to SFI funded computing resources at Tyndall Institute and the SFI/HEA funded Irish Centre for High End Computing. SR and MN are thankful to the COST Action CM1104 "Reducible Metal Oxides, Structure and Function" for the support. DH acknowledges "Movilidad UVA-BANCO SANTANDER 2019" mobility program for funding her research work at IT Sligo. CR-P participation in this work has been sponsored by the research initiative "Cátedra de Conocimiento e Innovación" from "Caja Rural de Soria" (Spain).

References:

1. Kumaravel V, Mathew S, Bartlett J, Pillai SC. Photocatalytic hydrogen production using metal doped TiO₂: A review of recent advances. Applied Catalysis B: Environmental. 2019;244:1021-64.

2. Binas V, Papadaki D, Maggos T, Katsanaki A, Kiriakidis G. Study of innovative photocatalytic cement based coatings: The effect of supporting materials. *Construction and Building Materials*. 2018;168:923-30.
3. Koivisto AJ, Kling KI, Fonseca AS, Bluhme AB, Moreman M, Yu M, et al. Dip coating of air purifier ceramic honeycombs with photocatalytic TiO₂ nanoparticles: A case study for occupational exposure. *Science of the Total Environment*. 2018;630:1283-91.
4. Gandolfo A, Rouyer L, Wortham H, Gligorovski S. The influence of wall temperature on NO₂ removal and HONO levels released by indoor photocatalytic paints. *Applied Catalysis B: Environmental*. 2017;209:429-36.
5. Athanasekou CP, Moustakas NG, Morales-Torres S, Pastrana-Martínez LM, Figueiredo JL, Faria JL, et al. Ceramic photocatalytic membranes for water filtration under UV and visible light. *Applied Catalysis B: Environmental*. 2015;178:12-9.
6. Jo S-H, Kim K-H, Kim Y-H, Lee M-H, Kim B-W, Ahn J-H. Deodorization of food-related nuisances from a refrigerator: The feasibility test of photocatalytic system. *Chemical Engineering Journal*. 2015;277:260-8.
7. Abdelhameed RM, Kamel OM, Amr A, Rocha Jo, Silva AM. Antimosquito activity of a titanium-organic framework supported on fabrics. *ACS applied materials & interfaces*. 2017;9(27):22112-20.
8. Leyland NS, Podporska-Carroll J, Browne J, Hinder SJ, Quilty B, Pillai SC. Highly efficient F, Cu doped TiO₂ anti-bacterial visible light active photocatalytic coatings to combat hospital-acquired infections. *Scientific reports*. 2016;6:24770.
9. Yemmireddy VK, Hung YC. Using photocatalyst metal oxides as antimicrobial surface coatings to ensure food safety—Opportunities and challenges. *Comprehensive Reviews in Food Science and Food Safety*. 2017;16(4):617-31.
10. Xia X, Peng S, Bao Y, Wang Y, Lei B, Wang Z, et al. Control of interface between anatase TiO₂ nanoparticles and rutile TiO₂ nanorods for efficient photocatalytic H₂ generation. *Journal of Power Sources*. 2018;376:11-7.
11. Maity P, Mohammed OF, Katsiev K, Idriss H. Study of the bulk charge carrier dynamics in anatase and rutile TiO₂ single crystals by femtosecond time-resolved spectroscopy. *The Journal of Physical Chemistry C*. 2018;122(16):8925-32.
12. Dubey R. Temperature-dependent phase transformation of TiO₂ nanoparticles synthesized by sol-gel method. *Materials Letters*. 2018;215:312-7.
13. Hanaor DA, Sorrell CC. Review of the anatase to rutile phase transformation. *Journal of Materials science*. 2011;46(4):855-74.
14. Fagan R, Synnott DW, McCormack DE, Pillai SC. An effective method for the preparation of high temperature stable anatase TiO₂ photocatalysts. *Applied Surface Science*. 2016;371:447-52.

15. Shirai K, Fazio G, Sugimoto T, Selli D, Ferraro L, Watanabe K, et al. Water-assisted hole trapping at the highly curved surface of nano-TiO₂ photocatalyst. *Journal of the American Chemical Society*. 2018;140(4):1415-22.
16. Xu F, Zhang J, Zhu B, Yu J, Xu J. CuInS₂ sensitized TiO₂ hybrid nanofibers for improved photocatalytic CO₂ reduction. *Applied Catalysis B: Environmental*. 2018;230:194-202.
17. Jia T, Fu F, Yu D, Cao J, Sun G. Facile synthesis and characterization of N-doped TiO₂/C nanocomposites with enhanced visible-light photocatalytic performance. *Applied Surface Science*. 2018;430:438-47.
18. Kernazhitsky L, Shymanovska V, Gavrilko T, Naumov V, Fedorenko L, Baran J. Dark-blue titanium dioxide: Effect of phenothiazine on structural and optical properties of nanocrystalline anatase TiO₂. *Journal of Physics and Chemistry of Solids*. 2019;126:234-41.
19. Xu M, Gao Y, Moreno EM, Kunst M, Muhler M, Wang Y, et al. Photocatalytic activity of bulk TiO₂ anatase and rutile single crystals using infrared absorption spectroscopy. *Physical Review Letters*. 2011;106(13):138302.
20. Yin W-J, Wen B, Zhou C, Selloni A, Liu L-M. Excess electrons in reduced rutile and anatase TiO₂. *Surface Science Reports*. 2018;73(2):58-82.
21. Khatun N, Tiwari S, Vinod C, Tseng C-M, Wei Liu S, Biring S, et al. Role of oxygen vacancies and interstitials on structural phase transition, grain growth, and optical properties of Ga doped TiO₂. *Journal of Applied Physics*. 2018;123(24):245702.
22. Gaur LK, Kumar P, Kushavah D, Khiangte KR, Mathpal MC, Agrahari V, et al. Laser induced phase transformation influenced by Co doping in TiO₂ nanoparticles. *Journal of Alloys and Compounds*. 2019;780:25-34.
23. Byrne C, Moran L, Hermosilla D, Merayo N, Blanco Á, Rhatigan S, et al. Effect of Cu Doping on the Anatase-to-Rutile Phase Transition in TiO₂ Photocatalysts: Theory and Experiments. *Applied Catalysis B: Environmental*. 2019; 246: 266-76.
24. Nolan NT, Seery MK, Pillai SC. Spectroscopic investigation of the anatase-to-rutile transformation of sol–gel-synthesized TiO₂ photocatalysts. *The Journal of Physical Chemistry C*. 2009;113(36):16151-7.
25. da Silva LF, Avansi Jr W, Catto AC, Rodrigues JE, Bernardi MI, Mastelaro VR. The Role of Nb Addition in TiO₂ Nanoparticles: Phase Transition and Photocatalytic Properties. *physica status solidi (a)*. 2018;215(21):1800321.
26. Zanatta A, Scoca D, Alvarez F. Influence of the Anatase and Rutile phases on the luminescent properties of rare-earth-doped TiO₂ films. *Journal of Alloys and Compounds*. 2019;780:491-7.
27. Loan TT, Long NN. Effect of Co²⁺ doping on Raman spectra and the phase transformation of TiO₂: Co²⁺ nanowires. *Journal of Physics and Chemistry of Solids*. 2019;124:336-42.

28. Zou K, Dong G, Liu J, Xu B, Wang D. Effects of calcination temperature and Li⁺ ions doping on structure and upconversion luminescence properties of TiO₂: Ho³⁺-Yb³⁺ nanocrystals. *Journal of materials science & technology*. 2019;35(4):483-90.
29. Arantes DC, de Mayrinck C, Santos JD, Maia LF, Oliveira LF, Schiavon MA, et al. Effect of structural and Eu³⁺ amount in TiO₂ semiconductor material on downconversion photoluminescence properties. *Optical Materials*. 2019;88:522-33.
30. Suwannaruang T, Kidkhunthod P, Chanlek N, Soontaranon S, Wantala K. High anatase purity of nitrogen-doped TiO₂ nanorice particles for the photocatalytic treatment activity of pharmaceutical wastewater. *Applied Surface Science*. 2019; 478:1-14.
31. Zikriya M, Nadaf Y, Bharathy PV, Renuka C. Luminescent characterization of rare earth Dy³⁺ ion doped TiO₂ prepared by simple chemical co-precipitation method. *Journal of Rare Earths*. 2019;37(1):24-31.
32. Feltrin J, De Noni Jr A, Hotza D, Frade J. Design guidelines for titania-silica-alumina ceramics with tuned anatase to rutile transformation. *Ceramics International*. 2019; 45(5): 5179-88.
33. Miljević B, van der Bergh J, Vučetić S, Lazar D, Ranogajec J. Molybdenum doped TiO₂ nanocomposite coatings: Visible light driven photocatalytic self-cleaning of mineral substrates. *Ceramics International*. 2017;43(11):8214-21.
34. Zhang T, Yu B, Wang D, Zhou F. Molybdenum-doped and anatase/rutile mixed-phase TiO₂ nanotube photoelectrode for high photoelectrochemical performance. *Journal of Power Sources*. 2015;281:411-6.
35. Erdogan N, Park J, Ozturk A. Synthesis and enhanced photocatalytic activity of molybdenum, iron, and nitrogen triple-doped titania nanopowders. *Ceramics International*. 2016;42(15):16766-74.
36. Khan M, Xu J, Cao W, Liu Z-K. Mo-Doped TiO₂ with Enhanced Visible Light Photocatalytic Activity: A Combined Experimental and Theoretical Study. *Journal of Nanoscience and Nanotechnology*. 2014;14(9):6865-71.
37. Zhou J, Feng B, Lu X, Duan K. Novel one-step fabrication of highly ordered Mo-doped TiO₂ nanotubes arrays with enhanced visible light catalytic activity. *Journal of Materials Science: Materials in Electronics*. 2018;29(21):18388-96.
38. Khan H, Berk D. Characterization and mechanistic study of Mo⁺⁶ and V⁺⁵ codoped TiO₂ as a photocatalyst. *Journal of Photochemistry and Photobiology A: Chemistry*. 2014;294:96-109.
39. Kemp TJ, McIntyre RA. Transition metal-doped titanium (IV) dioxide: Characterisation and influence on photodegradation of poly (vinyl chloride). *Polymer Degradation and Stability*. 2006;91(1):165-94.

40. Fisher L, Ostovapour S, Kelly P, Whitehead K, Cooke K, Storgårds E, et al. Molybdenum doped titanium dioxide photocatalytic coatings for use as hygienic surfaces: the effect of soiling on antimicrobial activity. *Biofouling*. 2014;30(8):911-9.
41. Yoon Y, Lee S, Gwon J, Cho H, Wu Q, Kim Y, et al. Photocatalytic performance of highly transparent and mesoporous molybdenum-doped titania films fabricated by templating cellulose nanocrystals. *Ceramics International*. 2018;44(14):16647-53.
42. Kresse G, Furthmüller J. Efficiency of Ab-initio Total Energy Calculations for Metals and Semiconductors using a Plane-wave Basis Set. *Computational Materials Science*. 1996;6(1):15-50.
43. Kresse G, Furthmüller J. Efficient Iterative Schemes for Ab-initio Total-energy Calculations using a Plane-wave Basis Set. *Physical Review B*. 1996;54(16):11169.
44. Kresse G, Joubert D. From ultrasoft pseudopotentials to the projector augmented-wave method. *Phys Rev B*. 1999;59(3):1758-75.
45. Blöchl PE. Projector augmented-wave method. *Phys Rev B*. 1994;50(24):17953-79.
46. Perdew JP, Burke K, Ernzerhof M. Generalized gradient approximation made simple. *Phys Rev Lett*. 1996;77(18):3865-8.
47. Rao KVK, Naidu SVN, Iyengar L. Thermal Expansion of Rutile and Anatase. *J Am Ceram Soc*. 1970;53(3):124-6.
48. Anisimov VI, Zaanen J, Andersen OK. Band theory and Mott insulators: Hubbard U instead of Stoner I. *Phys Rev B*. 1991;44(3):943-54.
49. Dudarev SL, Botton GA, Savrasov SY, Humphreys CJ, Sutton AP. Electron-energy-loss spectra and the structural stability of nickel oxide: An LSDA+U study. *Phys Rev B*. 1998;57(3):1505-9.
50. Nolan M, Elliott SD. The p-type conduction mechanism in Cu₂O: a first principles study. *Phys Chem Chem Phys*. 2006;8(45):5350-8.
51. Morgan BJ, Watson GW. A DFT + U description of oxygen vacancies at the TiO₂ rutile (1 1 0) surface. *Surf Sci*. 2007;601(21):5034-41.
52. Nolan M, Elliott SD, Mulley JS, Bennett RA, Basham M, Mulheran P. Electronic structure of point defects in controlled self-doping of the TiO₂ (110) surface: Combined photoemission spectroscopy and density functional theory study. *Phys Rev B*. 2008;77(23):235424.
53. Kowalski PM, Camellone MF, Nair NN, Meyer B, Marx D. Charge Localization Dynamics Induced by Oxygen Vacancies on the TiO₂ (110) Surface. *Phys Rev Lett*. 2010;105(14):146405.

54. Wu M, Yao X, Hao Y, Dong H, Cheng Y, Liu H, et al. Electronic structures, magnetic properties and band alignments of 3d transition metal atoms doped monolayer MoS₂. *Phys Lett A*. 2018;382(2):111-5.
55. Henkelman G, Arnaldsson A, Jónsson H. A fast and robust algorithm for Bader decomposition of charge density. *Computational Materials Science*. 2006;36(3):354-60.
56. Hatchard C, Parker CA. A new sensitive chemical actinometer-II. Potassium ferrioxalate as a standard chemical actinometer. *Proceedings of the Royal Society of London Series A Mathematical and Physical Sciences*. 1956;235(1203):518-36.
57. Montalti M, Credi A, Prodi L, Gandolfi MT. *Handbook of photochemistry*: CRC press; 2006.
58. Lange B, Strathmann M, Oßmer R. Performance validation of chromogenic coliform agar for the enumeration of *Escherichia coli* and coliform bacteria. *Letters in applied microbiology*. 2013;57(6):547-53.
59. Kumaravel V, Rhatigan S, Mathew S, Bartlett J, Nolan M, Hinder SJ, et al. Indium Doped TiO₂ Photocatalysts with High Temperature Anatase Stability. *The Journal of Physical Chemistry C*. 2019; 123(34):21083-96.
60. Pillai SC, Periyat P, George R, McCormack DE, Seery MK, Hayden H, et al. Synthesis of high-temperature stable anatase TiO₂ photocatalyst. *The Journal of Physical Chemistry C*. 2007;111(4):1605-11.
61. Fagan R, McCormack DE, Hinder S, Pillai SC. Improved high temperature stability of anatase TiO₂ photocatalysts by N, F, P co-doping. *Materials & Design*. 2016;96:44-53.
62. Byrne C, Rhatigan S, Hermosilla D, Merayo N, Blanco Á, Michel MC, et al. Modification of TiO₂ with hBN: high temperature anatase phase stabilisation and photocatalytic degradation of 1, 4-dioxane. *Journal of Physics: Materials*. 2019;3(1):015009.
63. Yu X, Hou T, Sun X, Li Y. The Influence of Defects on Mo-Doped TiO₂ by First-Principles Studies. *ChemPhysChem*. 2012;13(6):1514-21.
64. Liu G, Wang L, Yang HG, Cheng H-M, Lu GQM. Titania-based photocatalysts—crystal growth, doping and heterostructuring. *Journal of Materials Chemistry*. 2010;20(5):831-43.
65. Thi TV, Rai AK, Gim J, Kim S, Kim J. Effect of Mo⁶⁺ doping on electrochemical performance of anatase TiO₂ as a high performance anode material for secondary lithium-ion batteries. *Journal of Alloys and Compounds*. 2014;598:16-22.
66. Zhang J, Xi J, Ji Z. Mo⁺ N codoped TiO₂ sheets with dominant {001} facets for enhancing visible-light photocatalytic activity. *Journal of materials chemistry*. 2012;22(34):17700-8.
67. López R, Gómez R. Photocatalytic degradation of 4-nitrophenol on well characterized sol-gel molybdenum doped titania semiconductors. *Topics in catalysis*. 2011;54(8-9):504-11.

68. Avilés-García O, Espino-Valencia J, Romero R, Rico-Cerda JL, Arroyo-Albiter M, Natividad R. W and Mo doped TiO₂: Synthesis, characterization and photocatalytic activity. *Fuel*. 2017;198:31-41.
69. Dorraj M, Goh BT, Sairi NA, Woi PM, Basirun WJ. Improved visible-light photocatalytic activity of TiO₂ co-doped with copper and iodine. *Applied Surface Science*. 2018;439:999-1009.
70. Tian F, Zhang Y, Zhang J, Pan C. Raman spectroscopy: a new approach to measure the percentage of anatase TiO₂ exposed (001) facets. *The Journal of Physical Chemistry C*. 2012;116(13):7515-9.
71. Avilés-García O, Espino-Valencia J, Romero-Romero R, Rico-Cerda J, Arroyo-Albiter M, Solís-Casados D, et al. Enhanced Photocatalytic Activity of Titania by Co-Doping with Mo and W. *Catalysts*. 2018;8(12):631.
72. Zhang H, Tan K, Zheng H, Gu Y, Zhang W. Preparation, characterization and photocatalytic activity of TiO₂ codoped with yttrium and nitrogen. *Materials Chemistry and Physics*. 2011;125(1-2):156-60.
73. Choudhury B, Choudhury A. Dopant induced changes in structural and optical properties of Cr³⁺ doped TiO₂ nanoparticles. *Materials Chemistry and Physics*. 2012;132(2-3):1112-8.
74. Santara B, Pal B, Giri P. Signature of strong ferromagnetism and optical properties of Co doped TiO₂ nanoparticles. *Journal of applied physics*. 2011;110(11):114322.
75. Parker J, Siegel R. Calibration of the Raman spectrum to the oxygen stoichiometry of nanophase TiO₂. *Applied Physics Letters*. 1990;57(9):943-5.
76. Sun L, Li J, Wang C, Li S, Chen H, Lin C. An electrochemical strategy of doping Fe³⁺ into TiO₂ nanotube array films for enhancement in photocatalytic activity. *Solar Energy Materials and Solar Cells*. 2009;93(10):1875-80.
77. Liu S-H, Syu H-R. One-step fabrication of N-doped mesoporous TiO₂ nanoparticles by self-assembly for photocatalytic water splitting under visible light. *Applied energy*. 2012;100:148-54.
78. Tripathi AK, Mathpal MC, Kumar P, Agrahari V, Singh MK, Mishra SK, et al. Photoluminescence and photoconductivity of Ni doped titania nanoparticles. *Advanced Materials Letters*. 2015;6(3):201-8.
79. Choudhury B, Choudhury A. Oxygen vacancy and dopant concentration dependent magnetic properties of Mn doped TiO₂ nanoparticle. *Current Applied Physics*. 2013;13(6):1025-31.
80. Ahmed S. Ferromagnetism in Cr-, Fe-, and Ni-doped TiO₂ samples. *Journal of Magnetism and Magnetic Materials*. 2017;442:152-7.

81. Yan Y, Zhou X, Lan J, Li Z, Zheng T, Cao W, et al. Efficient photocatalytic disinfection of *Escherichia coli* by N-doped TiO₂ coated on coal fly ash cenospheres. *Journal of Photochemistry and Photobiology A: Chemistry*. 2018;367:355-64.
82. Mecha A, Onyango M, Ochieng A, Momba M. UV and solar photocatalytic disinfection of municipal wastewater: Inactivation, reactivation and regrowth of bacterial pathogens. *International Journal of Environmental Science and Technology*. 2019;16(7):3687-96.
83. Venieri D, Fraggadaki A, Kostadima M, Chatzisyneon E, Binas V, Zachopoulos A, et al. Solar light and metal-doped TiO₂ to eliminate water-transmitted bacterial pathogens: Photocatalyst characterization and disinfection performance. *Applied Catalysis B: Environmental*. 2014;154:93-101.
84. You J, Guo Y, Guo R, Liu X. A review of visible light-active photocatalysts for water disinfection: Features and prospects. *Chemical Engineering Journal*. 2019; 373:624-641.
85. Vijay M, Ramachandran K, Ananthapadmanabhan P, Nalini B, Pillai B, Bondioli F, et al. Photocatalytic inactivation of Gram-positive and Gram-negative bacteria by reactive plasma processed nanocrystalline TiO₂ powder. *Current Applied Physics*. 2013;13(3):510-6.
86. Ganguly P, Byrne C, Breen A, Pillai SC. Antimicrobial Activity of Photocatalysts: Fundamentals, Mechanisms, Kinetics and Recent Advances. *Applied Catalysis B: Environmental*. 2018; 225:51-75.
87. Reddy PVL, Kavitha B, Reddy PAK, Kim K-H. TiO₂-based photocatalytic disinfection of microbes in aqueous media: a review. *Environmental research*. 2017;154:296-303.